Journal of *Marine Science and Engineering*

MDPI

Article

Comparative Study on Added Resistance and Seakeeping Performance of X-Bow and Wave-Piercing Monohull in Regular Head Waves

Shuling Chen [1,*], Beilei Zou [1], Changzhi Han [1] and Shiqiang Yan [2]

[1] School of Naval Architecture and Ocean Engineering, Jiangsu University of Science and Technology, Zhenjiang 212100, China; mowei08242021@163.com (B.Z.); hancz0906@163.com (C.H.)
[2] School of Mathematics, Computer Science and Engineering, City University of London, London EC1V 0HB, UK; shiqiang.yan@city.ac.uk
* Correspondence: chensl@just.edu.cn

Abstract: Bow shape has been recognized as an important factor influencing the seakeeping performance and added resistance of ships. This paper presents a numerical comparative study on added resistance and seakeeping of model ships with 'X-bow' and a wave-piercing monohull in regular head waves using a computational fluid dynamics (CFD) software. Different wave heights, wavelengths and forward speeds are considered in the systematic investigation in order to characterize the added resistance and wave-induced motions, and to explore the local wave patterns. The results show a considerably different hydrodynamic characteristic by different bow shapes.

Keywords: seakeeping; added resistance; X-bow; wave-piercing monohull; CFD

Citation: Chen, S.; Zou, B.; Han, C.; Yan, S. Comparative Study on Added Resistance and Seakeeping Performance of X-Bow and Wave-Piercing Monohull in Regular Head Waves. *J. Mar. Sci. Eng.* **2022**, *10*, 813. https://doi.org/10.3390/jmse10060813

Academic Editor: Md Jahir Rizvi

Received: 13 May 2022
Accepted: 10 June 2022
Published: 14 June 2022

1. Introduction

Following increasing demands on high-speed vessels, surface unmanned vehicles (USV) [1,2] and green (energy efficiency) ships, ship hull optimizations aiming for a good seakeeping performance and low added resistance become increasingly critical to meet the net-zero target.

Intensive studies have been conducted and revealed the importance of the bow shape optimization for the purpose of improving the seakeeping performance of and reducing the resistance on ships. For example, Gao et al. [3] carried out an experimental research on drag performance of the 'X-bow' and demonstrated its promising performance on drag reduction in the high-speed condition and a good seakeeping performance subjected to a certain speed range; White et al. [4] introduced an inverted V-bow to a warship porotype and observed a reduction in the acceleration but a more significant motion amplitude of the ship; Kuroda et al. [5] investigated three different bow shapes to assess their ultimate influence on powering and greenhouse emissions, which are closely relevant to the hull resistance; White [6] compared the original bow of the FFG-7 frigate and the inverted bow form in terms of the calm water resistance and seakeeping in both regular and irregular head sea. They concluded that the inverted bow form reduces the resistance and confirmed a similar observation by Kensett et al. [4], i.e., the inverted bow increases the hull motion but decreases the acceleration; Kim et al. [7] developed a so-called KWP-bow, which reduces the required power at the level of 5–15% depending on the wave height; Huang et al. [8] concluded that M-type trimaran has a better calm water resistance performance and seakeeping performance than the channel boat; Yu et al. [9] and Zhang et al. [10] studied the optimization of the bow shape for improving the seakeeping performance.

Such research has significantly contributed to the optimization of bow shape and the development of new bow types, such as the X-bow proposed by Ulstein company [11]. The X-bow has a unique shape inspired by nature. Unlike the conventional bow, which leans

forwards from the side view, the X-bow is curved backwards and extends the waterline to the full bow height. This increases the foreship volume and therefore reduces the impact loads in high sea state. From the front view, the conventional bow has a blunt angle, which pushes the water away, crushes the waves and generates spray; whereas the X-bow has a sharper angle, which splits the waves and thus distributes the load more evenly over the bow surface. It has been demonstrated that the X-bow results in smaller hull motions and thus improves the on-boat comfort and safety when subjected to a relatively low navigation speed [12]. However, its performance at high navigation speeds may be limited and needs more investigation. In fact, at high navigation speeds, the wave-piercing bow has demonstrated its effectiveness on improving the seakeeping and reducing the resistance, especially the slamming load. Wei et al. [13] studied the effect of the bow shape on hydrodynamic performance of a mono-craft with a slender wave-piercing bow in calm water. They observed a significant influence of the bow shape on resistance, hull motions and wave making for small-scale and/or high-speed problems. Begovic et al. [14] concluded that the accelerations, heave and pitch motion of the ship with wave-piercing design are smaller than that of the traditional hull. The reduction by the wave-piercing bow may be up to 40%, depending on the speed and sea conditions. Further studies may be required on the added resistance and seakeeping of the wave-piercing bow.

In this work, systematic numerical comparative study has been carried out to investigate the added resistance, wave-induced motions and local wave pattern associated with the X-bow and the wave-piercing monohull. The two-phase incompressible Navier–Stokes solver in the computational fluid dynamics (CFD) software, StarCCM+, is adopt in the investigation, considering the fact that the viscous/turbulent effects and breaking wave (green water) impact may be significant when the ship forwards at a high speed and/or subjected to extreme waves. The paper only considers regular head waves, building the foundation for our future work in irregular and/or oblique waves. It is also noted that the ship in head sea is expected to undergo wave-induced motions with three degrees of freedoms, i.e., surge, heave and pitch. For simplification, we prescribe the surge motion by giving the forwarding speed and only allow heave and pitch motions in the CFD work.

2. Mathematical and Numerical Approaches

2.1. Brief Introduction of StarCCM+ Solver

As indicated above, the problem associated with ships moving in a wave field is numerically investigated by the StarCCM+, which solves incompressible two-phase unsteady Reynolds Averaged Navier–Stokes equation using the finite volume method with the volume of fluid (VOF) technique to identify the free surface. The k–ε turbulence model is used for resolving the eddy viscosity. For the finite volume discretization, a second-order upwind scheme is used to deal with the convection terms and first order scheme is used for temporal discretization.

The dynamic fluid body interaction (DFBI) model is applied to solve the motion of the ship. In the DFBI, the pressure and shear forces over the surface of the ship is integrated to estimate the forces/moments, which are used to find the acceleration of the ship. By integrating the acceleration, the velocity and the displacement of the ship can be obtained. It is noted that solving the pressure and the velocity field in the fluid domain requires the boundary condition on the ship surface which depends on the motion of the ship. Therefore, an iterative procedure is required to decouple the mutual relation. More details of the CFD solver utilised by the StarCCM+ can be found in its technical manual. For completeness, a brief summary is given herein.

2.2. Computational Configuration and Computational Mesh

For realizing the forwarding ship in waves, two approaches are commonly used in literatures [15]. The first one is to directly move the ship at its forward speed in the wave field, being consistent with the towing tank tests. The other one is to approximate the forward speed by introduce a uniform current in the opposite direction of the ship

forwarding speed and the ship only moves at its wave-induced motion. By using the 1st approach, a large computational domain is required to accommodate the motion of the ship. As revealed by Gong et al. [15], these two approaches result in similar results for linear and small waves, but may lead to considerably different results in nonlinear waves. Such differences are caused by the interaction between the artificial current, induced to approximate the forward speed of the ship, and the wave in the 2nd approach, which is not desirable in the real scenario. Nevertheless, considering the fact that the error caused by the undesirable wave–current interaction needs a certain duration to be built up, and the fact that the 2nd approach can use much smaller computational domain and thus higher computational efficiency compared with the 1st approach, the 2nd approach is still the most popular approach for CFD modelling on forwarding ships in waves. In this work, we use the 2nd approach based on the satisfactory accuracy demonstrated by the validation study.

The computational domain and the boundaries are sketched in Figure 1 and the configuration of the boundaries are summarized in Table 1, where L is the length of the ship. Such arrangement is obtained by using our preliminary test aiming to eliminate the reflection from the side and downstream boundaries and to capture the Kelvin wave. Near the side and outlet boundaries, damping zones are utilized to deal with the reflection from these boundaries. One may notice from Figure 1 that a local domain surrounding the ship is defined and used to apply the overset mesh technique. The basic idea of the overset mesh technique is that a local mesh is generated surrounding the ship and a background mesh is generated covering the entire computational domain without the structures. During the simulation, the entire local mesh moves following the motion of the ship, a hole is cut in the background mesh to accommodate the instantaneous position of the local mesh. After the hole-cutting, the background mesh has an overlap zone with the local mesh, in which an appropriate interpolation function is applied for transition of the solutions between two mesh. It is important to note that there is no mesh deformation during the above-mentioned procedure. This overcomes the mesh distortion occurs in the computational mesh with the conventional dynamic mesh technique, in which the computational mesh moves in order to conform to the motion of the ship, in the cases with large motion of the ship. The size of the local zone is chosen as $1.4\,L \times 0.2\,L \times 0.4\,L$. The problems to be considered in this paper, i.e., forwarding ships in head sea, are symmetrical about the longitudinal central plane, only half of the computational domain with a symmetry boundary condition is considered in the present work, as illustrated in Figure 2a,b. After simulation is completed, the results can be reconstructed by symmetrical projection, as demonstrated by Figure 2d, which shows the free surface mesh after reconstruction.

Table 1. Configuration of the numerical domain.

Boundary	Position	Boundary Condition
Inlet	2 L in front of the ship	Velocity inlet
Outlet	5 L behind a ship	Pressure outlet
Symmetry	Symmetry plane of a ship	Symmetry
Side	2 L from symmetry plane	Velocity inlet
Top	1.5 L above free surface	Velocity inlet
Bottom	2 L below free surface	Velocity inlet

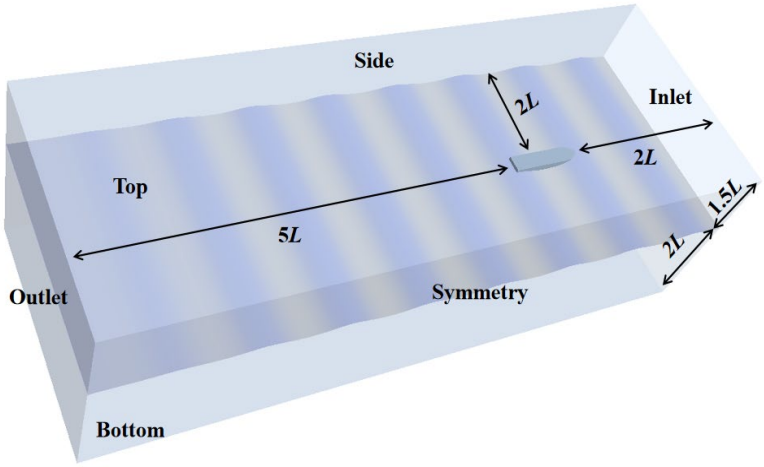

Figure 1. Sketch of the computational domain and boundaries.

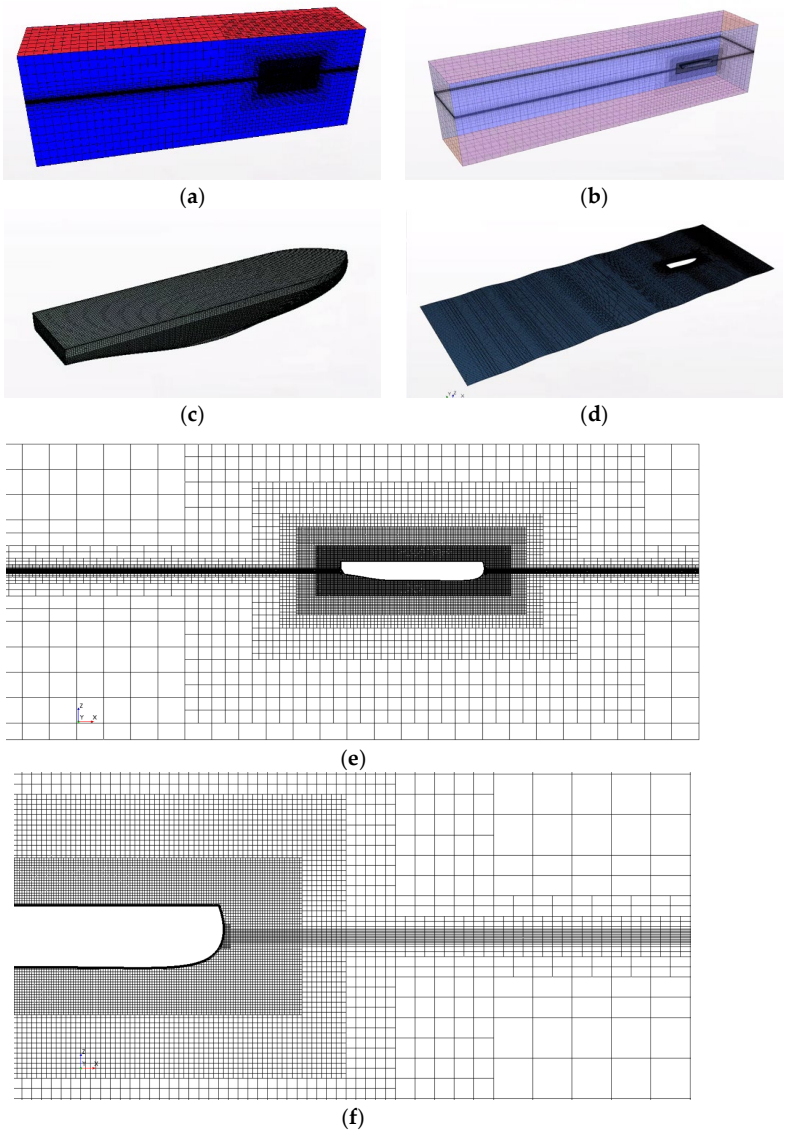

Figure 2. Illustrations of computational mesh; (**a**) Volumatic mesh **(b)** Surface mesh on boundaries (**c**) Surface mesh on the hull (**d**) Reconstructed free surface mesh (**e**) The overall mesh of computational domain (**f**) Local mesh in computational domain.

It is well known that sufficient mesh resolution is required to ensure convergence of the numerical solutions. For the free surface problems, ITTC [16] recommends at least 40 grid points over one wavelength of the shortest wave component when 2nd order spatial accuracy is used; StarCCM+ suggests a resolution of 80 points per wavelength and 15 per wave height. In this paper, 10–20 grid points per wave height and 60–120 points per wavelength are considered for the mesh in a confined zone near the free surface (Figure 2a). The mesh becomes gradually finer when approaches the hull surface and the finest mesh size is determined by appropriate y+ value. The mesh gradually becomes coarser in the area away from the free surface and/or the ship surface, as illustrated in Figure 2. The cells are mainly hexahedral with exception in the area near the ship surface, where prism cells are applied in order to well capture the boundary layer on the ship surface. In terms of the time step sizes, the Courant–Friedrich–Lewy (CFL) is used as a guideline. For seakeeping problems considered in this paper, the maximum Courant number for cells near the free surface is taken as 0.5. By considering the recommended mesh resolution indicated above, such CFL condition can be rewritten as $\Delta t = T/2.4n$, where T is wave period and n is number of grid points per wavelength, as recommended by StarCCM+ manual and adopted by this work.

2.3. Validations

Due to the fact that the corresponding experimental results of the X-bow and wave-piercing monohull are not available, the numerical validation is carried out by using the Wigley-III model, which is widely applied for benchmarking and validating numerical model, attributing to its mathematically defined geometry as follows,

$$\eta = \left(1-\zeta^2\right) \cdot \left(1-\xi^2\right) \cdot \left(1+a_2 \cdot \xi^2 + a_4 \cdot \xi^4\right) + \alpha \cdot \zeta^2 \cdot \left(1-\zeta^8\right) \cdot \left(1-\xi^2\right)^4 \quad (1)$$

which is written using the body fixed right-hand coordinate $O(\xi, \eta, \zeta)$. The origin O of the coordinate system located at the centre of the midship section and the mean water surface. ξ is the longitudinal axis pointing forwards. η is a lateral axis pointing towards the port side. ζ is a vertical axis pointing downwards. The coefficients $a_2 = 0.2, a_4 = 0, \alpha = 0$ are considered. The characteristic dimensions of the Wigley Hull are summarized in Table 2 and the geometry is illustrated in Figure 3.

Table 2. Characteristic dimensions of the Wigley hull.

Wigley Model	Wigley-III
Length to breadth ratio, L/B $(-)$	10
Length, L (m)	3.0000
Breadth, B (m)	0.3000
Draught, d (m)	0.1875
Trim, t (m)	0.0000
displacement, ∇ (m^3)	0.078
Centre of gravity above base, $\overline{KG}$ (m)	0.1700
Radius of inertia for pitch, k_{yy} (m)	0.7500

The test conditions of the Wigley-III hull model to be considered for validation are summarized in Table 3, in which λ is the wavelength. Figure 4 compares the heave motion amplitude (ξ_3), pitch motion amplitude (ξ_5) and added resistance (R_{aw}) of the Wigley-III between the numerical and experimental results [17]. For convenience, they are given in dimensionless forms, i.e., ξ_3/a, ξ_5/a and $\frac{R_{aw}}{\rho g a^2 B^2/L}$, where a and k are the wave amplitude and wave number, respectively, B is breadth of the ship, ρ is the density of the water and g the gravitational acceleration. ξ_3 and ξ_5 are obtained by FFT using the time histories of the heave and pitch motions at quasi-steady state where regular oscillation appears. The added resistance is obtained by the resistance in the wave field minus the corresponding resistance in the calm water at the same forward speed. Figure 4 demonstrates a satisfactory numerical

result, which agrees with the experimental results. The maximum relative difference for the cases shown in Figure 4 is 12.16%.

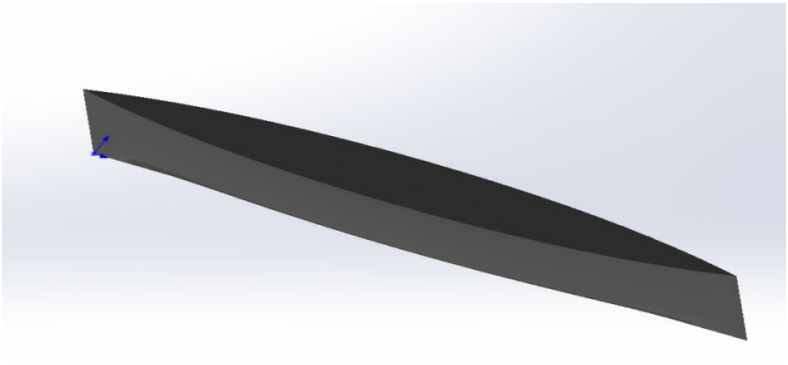

Figure 3. Sketch of the Wigley model.

Table 3. Test condition of Wigley-III hull model in head waves.

Case Name	Hull Form	*Fr*	*λ*/*L*	Wave Height *H*(m)
Case 1	Wigley-III	0.4	0.5	0.04
Case 2		0.4	1	0.04
Case 3		0.4	1.5	0.04
Case 4		0.4	2	0.04

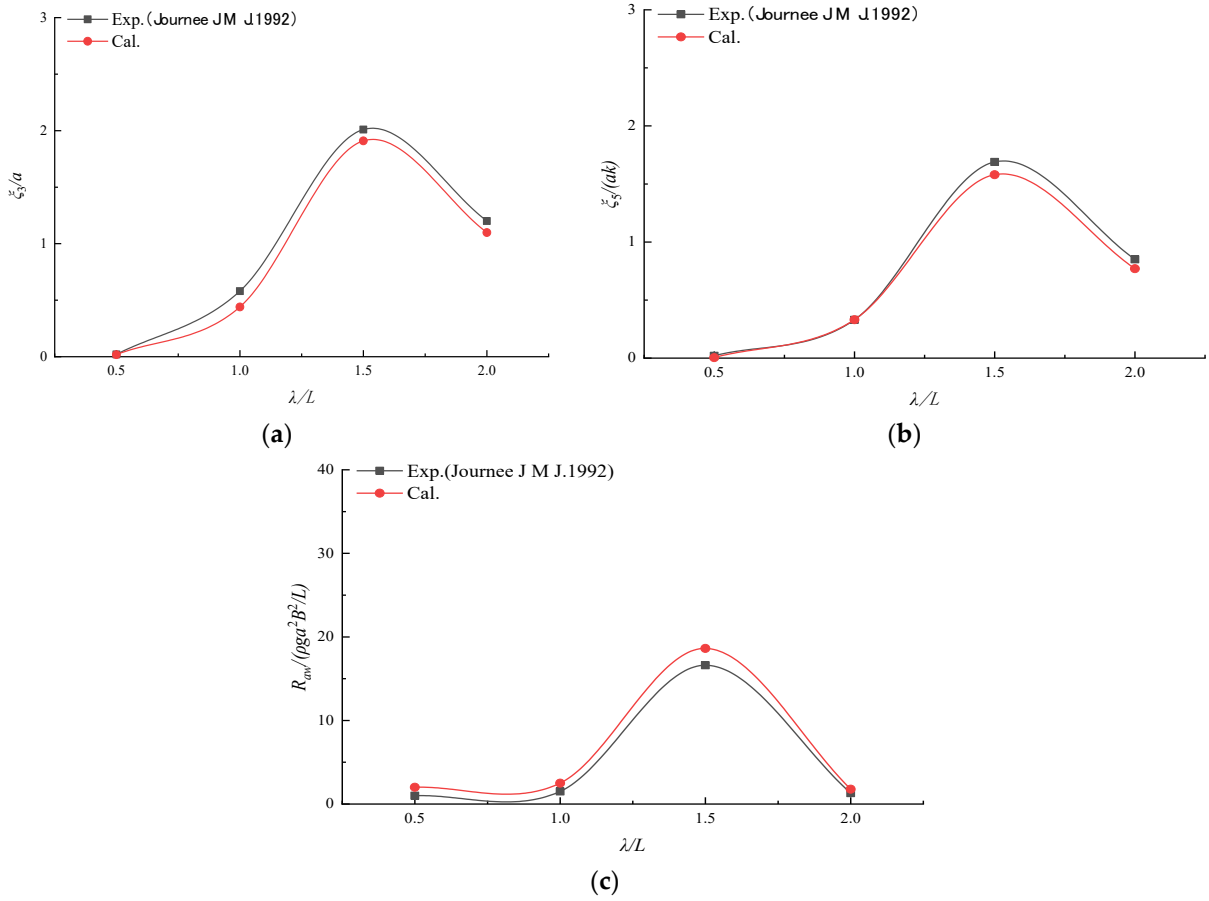

Figure 4. Comparison of (**a**) heave, (**b**) pitch and (**c**) added resistance coefficient of Wigley-III in head wave between the numerical and experimental results [17].

3. Numerical Configuration and Verification

As indicated above, the main purpose of this paper is to compare the X-bow and a wave-piercing bow in terms of seakeeping performance and added resistance. The original hull form (referred to as XB1) is taken from Niklas et al. [12]. The section lines of XB1 are sketched in Figure 5a. In order to improve the seaworthiness and to investigate the effect of the bow shape on the seakeeping and added resistance, the bow shape is modified by introducing a wave-piercing bow type in this study. The modified version is referred to as XW1 in this paper. The corresponding section lines of the XW1 are sketched in Figure 5b. The main dimensions of XB1 and XW1 are summarized in Table 4. It is noted that the shape of the stern and mid-ship together with the main dimensions, displacement, waterline length, draft and wetted surface are well preserved in the modification, and therefore, different numerical results between the cases with XB1 and the corresponding cases with XW1 can be largely attributed to the effect of the bow shape.

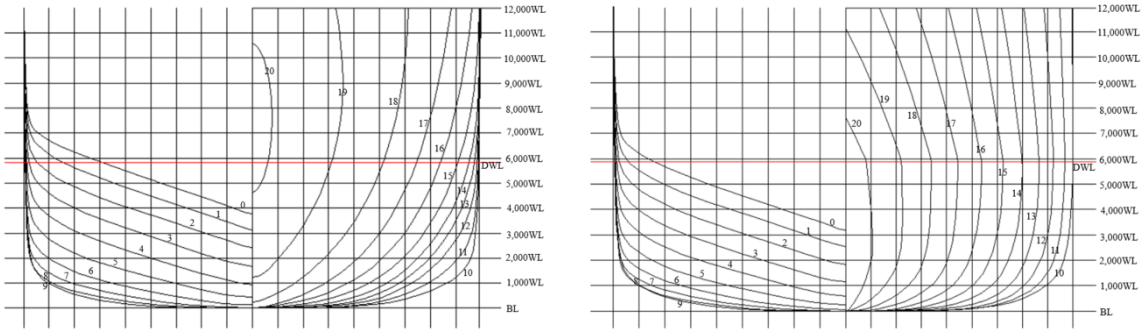

(**a**) (**b**)

Figure 5. Sketches of the section lines for XB1 and XW1 models; (**a**) XB1 (**b**) XW1.

Table 4. Main dimensions of ship models.

Name	XB1	XW1
Displacement, V (m^3)	0.0241	0.02664
Waterline length, L (m)	1.58	1.6
Breadth, B (m)	0.34	0.34
Draught, T (m)	0.1137	0.1137
Wetted surface, A (m^2)	0.46016	0.51642
Radius of inertia for pitch, k_{yy} (m)	0.401	0.401

In this paper, only regular waves in head sea with different wavelengths (λ/L = 0.8~2.5) and wave heights (H = 0.04 m, 0.08 m and 0.12 m) are considered. These waves are generated by using 5th order Stokes wave model. Two forwarding speeds, represented by Froude number ($Fr = v/\sqrt{gL}$) 0.3 and 0.5 are considered. All the test conditions are shown in Table 5.

Table 5. Summary of test conditions.

Hull Form	XB1 and XW1
Fr	0.3, 0.5
Wave height, H (m)	0.04, 0.08, 0.12
Ratio λ/L (−)	0.8, 1, 1.2, 1.5, 1.8, 2, 2.2, 2.5

Although Section 2.3 has demonstrated a promising accuracy of the present numerical procedure on numerically modelling the seakeeping and added resistance of a forwarding Wigley hull, a further convergence investigation is carried out for all cases associated with XB1 and XW1 in order to minimize the numerical uncertainty. Some results are presented here for demonstrations. In this case, XW1 model with forwarding speed at

Fr = 0.3 navigates in a head wave with the length ratio of $\lambda/L = 1$ and the wave height of 0.04 m (yielding a wave steepness $ak = 0.0253$). Three sets of mesh, which is summarized in Table 6, are used for the simulations. Following ITTC et al. [18], the mesh is refined by reducing the cell sizes through changing the number of $\lambda/\Delta x$ in the horizontal direction and $H_W/\Delta z$ (H_W is the wave height) in the vertical direction. The corresponding cell numbers of the Fine (G_1), Medium (G_2) and Coarse (G_3) meshes are 3.16×10^6, 1.36×10^6 and 0.61×10^6.

Table 6. Grids used for convergence tests for XW1 model.

Grid name	Hull form	Mesh	$\lambda/\Delta x$	$H_w/\Delta z$
G_1	'XW1'	Fine	120	12
G_2		Medium	84	8
G_3		Coarse	60	6

The results for the cases will also be used to perform the error and uncertainty analysis using the procedure recommended by ITTC [18]. For this purpose, the gird refinement ratio is kept at a constant with $r_G = \sqrt{2}$, as shown in Table 3, in which the first order Richardson extrapolation δ^*_{REG4}, accuracy order p_G, correction factor C_G and gird uncertainty U_G are calculated by:

$$R_G = \frac{\varepsilon_{G21}}{\varepsilon_{G32}} \tag{2}$$

$$p_G = \frac{\ln[(\varepsilon_{G32})/(\varepsilon_{G21})]}{\ln r_G} \tag{3}$$

$$\delta^*_{REG4} = \left(\frac{\varepsilon_{G21}}{r_G^{PG} - 1}\right) \tag{4}$$

$$C_G = \frac{r_G^{PG} - 1}{r_G^{PG_{est}} - 1} \tag{5}$$

$$U_G = |C_G \delta^*_{REG}| + |(1 - C_G)\delta^*_{REG}| \tag{6}$$

where $P_{Gest} = 2$ is used in Equation (5), $\varepsilon_{Gij} = f_{Gi} - f_{Gj}$ is the difference between f_{Gi} and f_{Gj}, and f_{Gi} is the computed result by Grid G_i.

The dimensionless amplitudes of the heave, pitch motion and the added resistance obtained by using different meshes are displayed in Figure 6, which clearly show a convergent trend for all three parameters when mesh size decreases. One may agree that the Medium mesh is sufficient for achieving reliable results for further analysis. Table 7 outlines the error and results of the grid uncertainty analysis calculated by Equations (2)–(6). It can be seen that the uncertainty of all the cases is less than 7.896%, which is considered as acceptable.

Table 7. Results of error and uncertainty analysis.

	r_G	p_G	C_G	δ^*_{REG}	R_G	U_G	U_G/f_G
$R_{aw}/(\rho g a^2 B^2/L)$	$\sqrt{2}$	7.49	12.408	0.006	0.075	0.133	7.986%
ξ_3/a	$\sqrt{2}$	8.857	20.53	0.00008474	0.0464	0.003395	0.962%
ξ_5/ak	$\sqrt{2}$	3.805	2.728	0.00195	0.2675	0.00875	3.305%

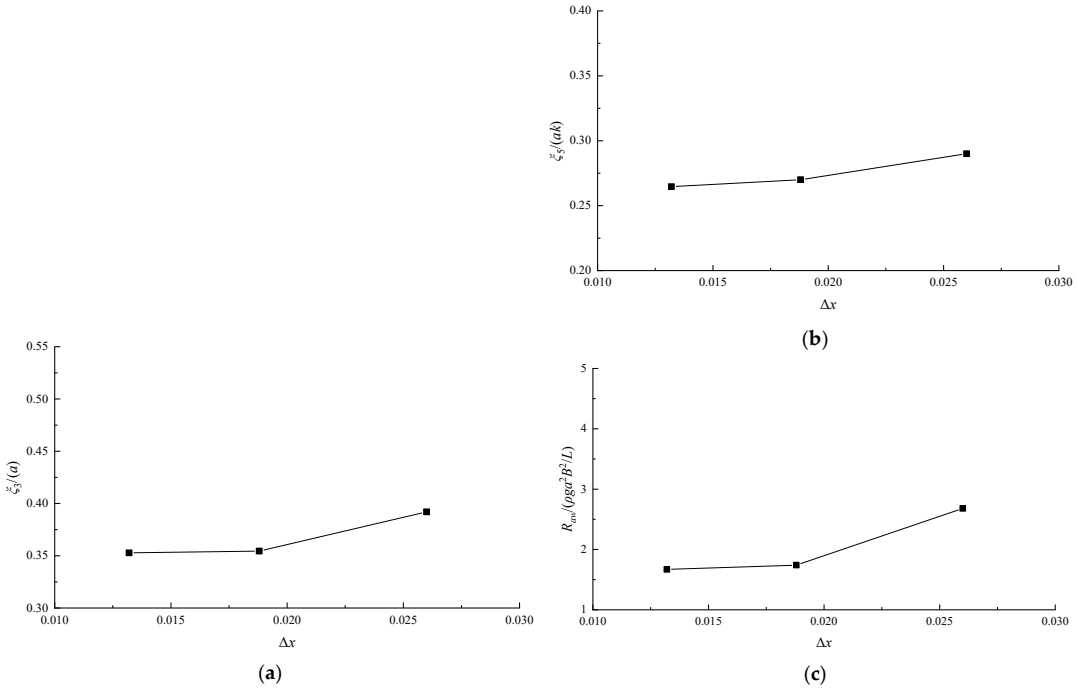

Figure 6. Grid convergence tests. (**a**) heave, (**b**) pitch and (**c**) added resistance.

4. Numerical Results and Discussions

On the basis of the convergence tests demonstrated above, systematic results on motion responses and added resistance of XB1 and XW1 are compared. Figure 7 shows the time histories of heave response, pitch response and resistance of hull (H = 0.12). Figure 8 displays the heave and pitch responses of these two hulls subjected to different wave conditions, whereas Figure 9 illustrates the corresponding values of the added resistance. Similarly to Figure 4, these are given in dimensionless forms.

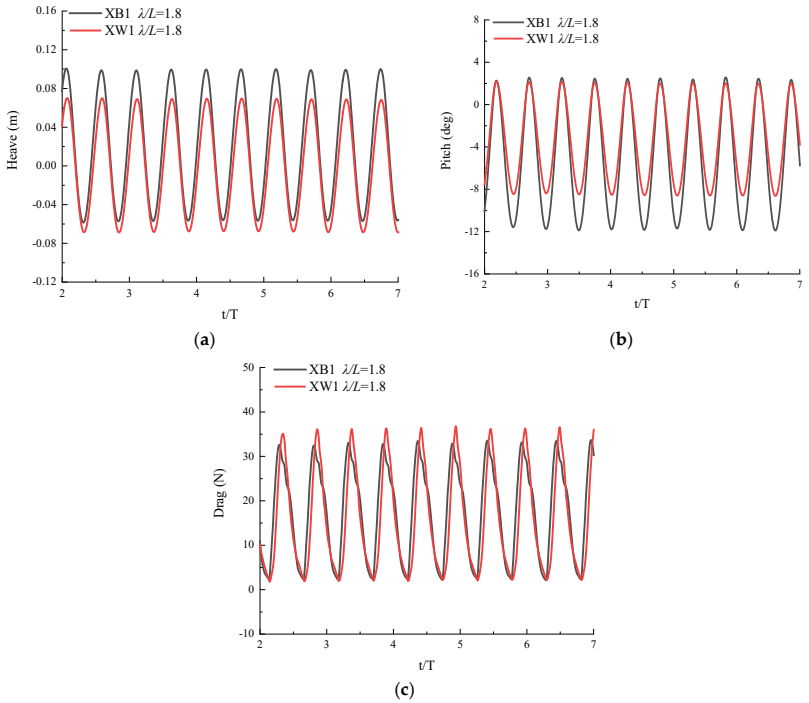

Figure 7. Time histories of heave response, pitch response and resistance of hull (H = 0.12); (**a**) Heave motion (**b**) Pitch motion (**c**) Resistance of hull.

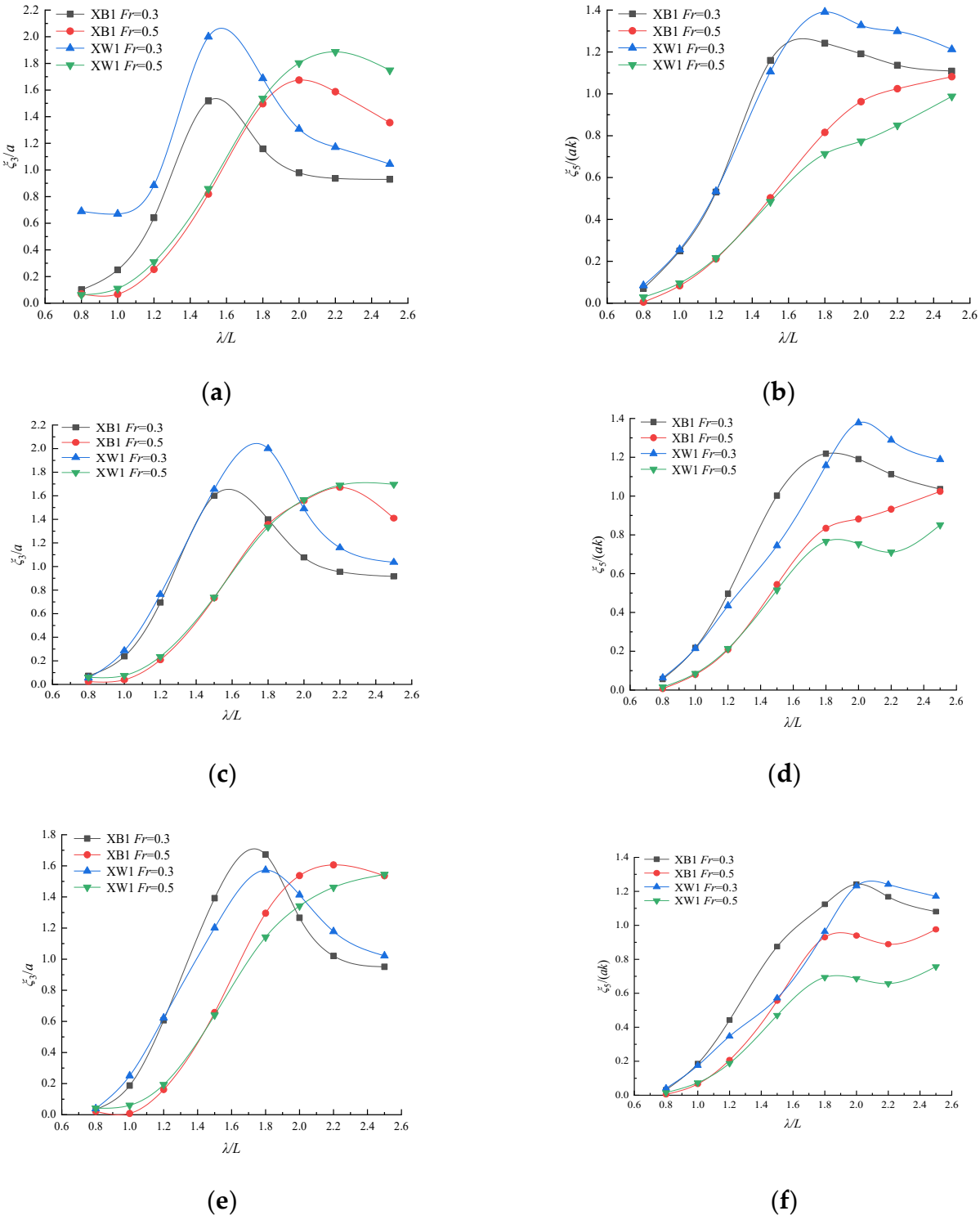

Figure 8. Heave and pitch responses of XB1 and XW1 subjected to different wave conditions; (**a**) Heave, H = 0.04 m (**b**) Pitch, H = 0.04 m (**c**) Heave, H = 0.08 m (**d**) Pitch, H = 0.08 m (**e**) Heave, H = 0.12 m (**f**) Pitch, H = 0.12 m.

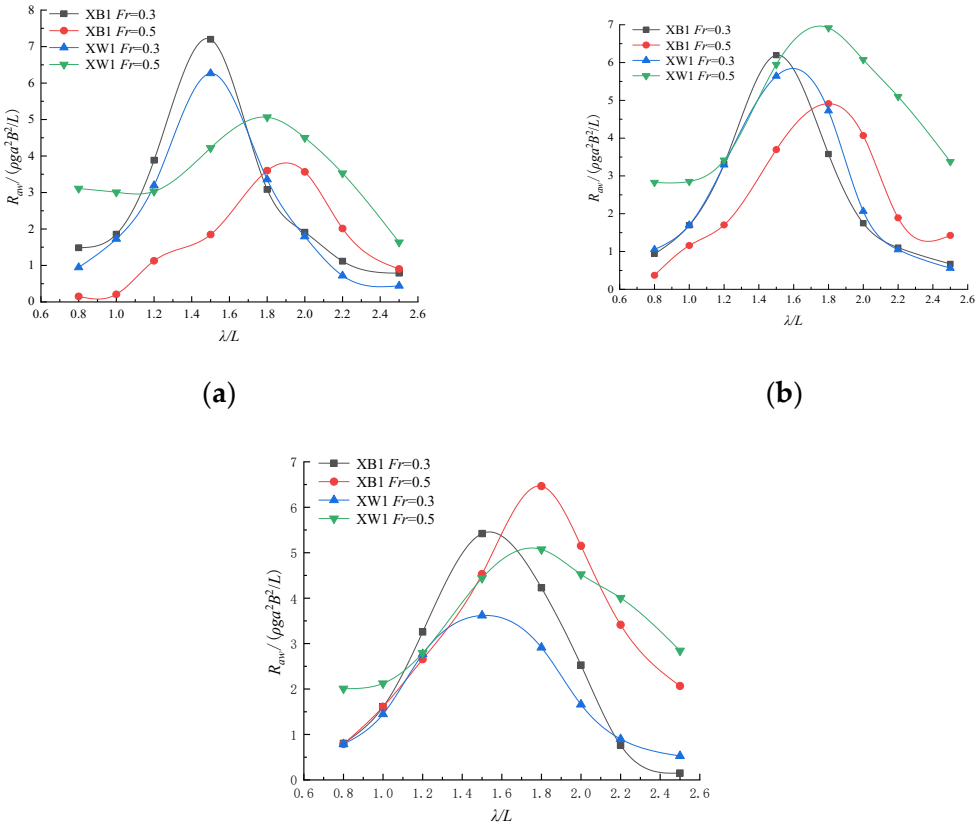

Figure 9. Computed results for 'XB1' and 'XW1' moving in waves with different wave conditions: (**a**) H = 0.04 (m), (**b**) H = 0.08 (m), (**c**) H = 0.12 (m).

Figure 8a,c,e present the heave responses for wave heights of 0.04 m, 0.08 m and 0.12 m, respectively. Compared with the X-bow (XB1), the wave-piercing bow (XW1) generally results in larger motion response for wide ranges of wavelengths considered in this paper, whereas in the cases with the largest wave height (H = 0.12), the wave-piercing bow (XW1) may lead to a smaller heave motion, especially for the cases with higher forwarding speed (Fr = 0.5) and longer waves (λ/L > 1.8), where the heave motion is significant. In most of the cases considered in this work, the effect of the bow shape in the heave responses is insignificant for short waves, i.e., λ/L < 1.6, expect for the cases with F_r = 0.3 and H = 0.04.

In terms of the pitch motions (Figure 8b,d,f), the wave-piercing bow (XW1) results in smaller pitch responses than the X-bow (XB1) in the cases with a higher forwarding speed (F_r = 0.5), whereas for a lower forwarding speed (F_r = 0.3), XW1 may yield larger motions for long waves, i.e., λ/L >1.6, 1.8 and 2.0 for H = 0.04 m, 0.08 m and 0.12 m, respectively.

From Figure 9, one can observe that for relatively small wave heights (i.e., H = 0.04 m and 0.08 m), the wave-piercing bow (XW1) results in considerably larger added resistance than the X-bow (XB1) in the cases with a high forwarding speed (Fr = 0.5); whereas it may lead to smaller added resistance in the cases with a low forwarding speed, despite the fact that the added resistance is not sensitive to the bow shape. For large waves, i.e., H = 0.12 m, wave-piercing bow (XW1) yields smaller added resistance for a specific range of λ/L, i.e., approximately 1.0 to 2.2 and 1.5 to 2.1 for the cases with Fr = 0.3 and 0.5, respectively.

Further details of the local flow pattern and the Kelvin wave fields are also explored in order to further explain the phenomenon in the hydrodynamics associated with the bow shapes causing the above-mentioned macroscopic performance in motion responses. Some results are shown below. Figure 10 shows the local flow pattern and Kelvin wave fields for

XB1 and XW1 with different lengths in head wave at F_r = 0.5. Obviously, the head wave is coupled with the wave generated by the ship model and the lanky Kelvin wave system is obvious. As the ship model is advancing in the mixed sea, the significant heave and pitch motions can be observed and the generated wave is close to the deck of the model, which leads to the green water event. On the other hand, it could be found that the wave height of XW1 is evidently reduced, which means that the wave energy losses of the flow field could be reduced with the X-bow.

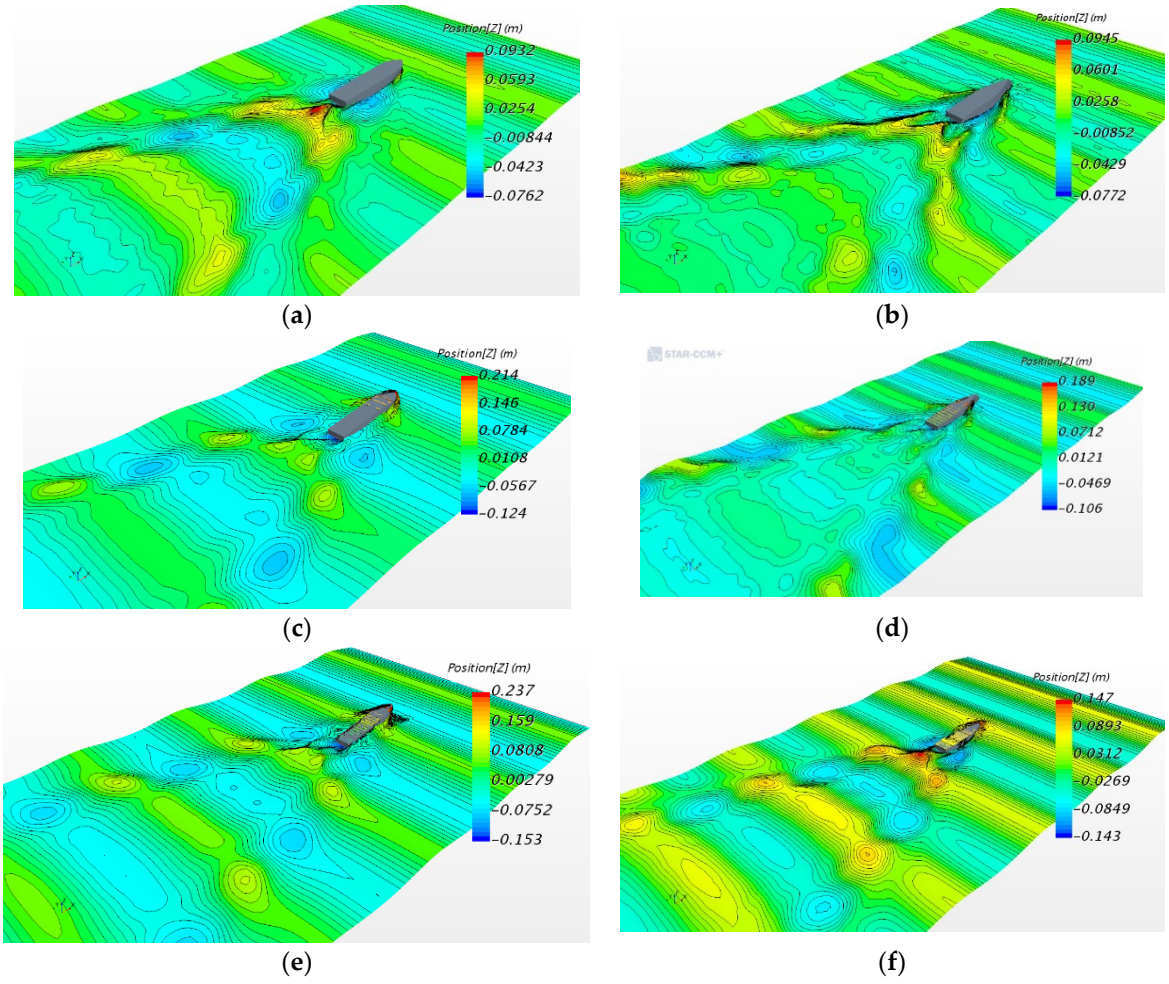

Figure 10. Local flow pattern and the Kelvin wave fields advancing at Fr = 0.5; (**a**) XB1 H = 0.04 (m) λ/L = 1.5 (**b**) XW1 H = 0.04 (m) λ/L = 1.5 (**c**) XB1 H = 0.08 (m) λ/L = 1.5 (**d**) XW1 H = 0.08 (m) λ/L = 1.5 (**e**) XB1 H = 0.12 (m) λ/L = 1.5 (**f**) XW1 H = 0.12(m) λ/L = 1.5.

5. Conclusions

The paper numerically investigates the added resistance and seakeeping performance of two types of bow shapes, i.e., the X-bow and the wave-piercing bow under different conditions. It uses CFD software StarCCM+ to conduct the investigation, after careful validation using the case with Wigley Hull and reliable mesh convergence test. The numerical results are concluded below,

When wave heights are small (i.e., H = 0.04 m and 0.08 m), the added resistance of ship model with the wave-piercing bow (XW1) is larger than the X-bow (XB1) in the cases with a high forwarding speed (Fr = 0.5), whereas the added resistance is not sensitive to the bow shape. For large waves, i.e., H = 0.12 m, the added resistance of ship model with wave-piercing bow (XW1) is smaller than the X-bow (XB1) for a specific range of λ/L, i.e., approximately 1.0 to 2.2 and 1.5 to 2.1 for the cases with Fr = 0.3 and 0.5, respectively.

The pitch responses of the ship model with the wave-piercing bow (XW1) are smaller than with the X-bow (XB1) in the cases with a higher forwarding speed (F_r = 0.5); whereas for a lower forwarding speed (Fr = 0.3), the XW1 may yield larger motions for long waves.

The wave-piercing bow (XW1) generally results in larger motion response for wide ranges of wavelengths considered in this paper, whereas in the cases with the largest wave height (H = 0.12), the wave-piercing bow (XW1) may lead to a smaller heave motion, especially for the cases with a higher forwarding speed (Fr = 0.5) and longer waves ($\lambda/L > 1.8$), where the heave motion is significant.

Although these results provide a good reference for bow shape optimization aiming for the net-zero target, further work is recommended to reveal more detailed hydrodynamics associated with these bow shapes, such as the green water occurrence, turbulence, etc. Irregular wave and oblique sea conditions will also be considered in future work.

Author Contributions: Conceptualization, S.C. and B.Z.; software, B.Z.; validation, B.Z. and C.H.; investigation, C.H.; data curation, C.H.; writing—original draft preparation, S.C. and B.Z.; writing—review and editing, S.Y.; visualization, B.Z.; project administration, S.C.; funding acquisition, S.C. All authors have read and agreed to the published version of the manuscript.

Funding: This research was funded by National Natural Science Foundation of China, 51409130.

Institutional Review Board Statement: Not applicable.

Informed Consent Statement: Not applicable.

Data Availability Statement: Not applicable.

Conflicts of Interest: The authors declare no conflict of interest.

References

1. Li, J. Development and Application of Unmanned Surface Vehicle. *Fire Control Command Control* **2012**, *37*, 203–207.
2. James, C. *Autonomous Mission Planning and Execution for Unmanned Surface Vehicles in Compliance with the Marine Rules of the Load*; University of Washington: Washington, DC, USA, 2007.
3. Gao, X.; Wu, Q.; Dong, Z. Model test research on the resistance performance of axe bow. In Proceedings of the 11th National Hydrodynamics Academic Conference, Wuxi, China, 19–24 October 2012.
4. White, J.K. Numerical and experimental investigation of the effect of an inverted bow on the hydrodynamic performance of navy combatant hull forms. *J. Appl. Log.* **2015**, *13*, 78–90.
5. Kuroda, M.; Tsujimoto, M.; Sasaki, N.; Ohmatsu, S.; Takagi, K. Study on the bow shapes above the waterline in view of the powering and greenhouse gas emissions in actual seas. *Proc. Inst. Mech. Eng. Part M J. Eng. Marit. Environ.* **2012**, *226*, 23–35. [CrossRef]
6. Yang, J.K.; Kim, Y. Numerical analysis of added resistance on blunt ships with different bow shapes in short waves. *J. Marine Sci. Technol.* **2017**, *22*, 245–258. [CrossRef]
7. Kim, Y.C.; Kim, K.S.; Kim, J.; Kim, Y.; Park, I.R.; Jang, Y.H. Analysis of added resistance and seakeeping responses in head sea conditions for low-speed full ships using URANS approach. *Int. J. Naval Arch. Ocean Eng.* **2017**, *9*, 641–654. [CrossRef]
8. Huang, W. Comparison of resistance and seakeeping between M-type boat and channel-type boat. *Ship Ocean. Eng.* **2015**, *44*, 56–69.
9. Yu, J.W.; Lee, C.M.; Lee, I.; Choi, J.E. Bow hull-form optimization in waves of a 66,000 DWT bulk carrier. *Int. J. Naval Arch. Ocean Eng.* **2017**, *9*, 499–508. [CrossRef]
10. Zhang, S.; Tezdogan, T.; Zhang, B.; Xu, L.; Lai, Y. Hull form optimisation in waves based on CFD technique. *Ships Offshore Struct.* **2018**, *13*, 149–164. [CrossRef]
11. Keuning, J.A.; Toxopeus, S.L.; Pinkster, J. The effect of bow shape on the seakeeping performance of a fast monohull. In Proceedings of the 6th International Conference on Fast Sea Transportation, Southampton, UK, 4–6 September 2001.
12. Niklas, K.; Pruszko, H. Full scale CFD seakeeping simulations for case study ship redesigned from V-shaped bulbous bow to X-bow hull form. *Appl. Ocean. Res.* **2019**, *89*, 188–201. [CrossRef]
13. Wei, C.Z.; Li, Y.H.; Yi, H. A comprehensive review on hull forms and relevant researches of wave piercing vessels. *Chin. J. Ship Res.* **2016**, *11*, 1–8.
14. Begovic, E.; Mancini, S. Stability and Seakeeping of Marine Vessels. *J. Mar. Sci. Eng.* **2012**, *9*, 222. [CrossRef]
15. Gong, J.; Yan, S.; Ma, Q.; Li, Y. Added resistance and seakeeping performance of trimarans in oblique waves. *Ocean. Eng.* **2020**, *216*, 107721. [CrossRef]
16. ITTC. *ITTC—Recommended Procedures and Guidelines—Practical Guidelines for Ship CFD Applications*; 7.5-03-02-03 (Revision 01); ITTC: Singapore, 2014; pp. 1–19.

17. Journee, I. *Experiments and Calculations on Four Wigley Hull Forms*; Faculty of Mechanical Engineering and Marine Technology—SHL Report 0909; Delft University of Technology: Delft, The Netherlands, 1992.
18. ITTC. Recommended Procedure and Guidelines, Uncertainty analysis in CFD verification and validation—Methodology and validation 7.5-03-01-01. In Proceedings of the 28th International Towing Tank Conference, Wuxi, China, 17–22 September 2017.